

ERS-1 Radar and Field-Observed Characteristics of Autumn Freeze-up in the Weddell Sea

Mark R. Drinkwater[†]

Jet Propulsion Laboratory
California Institute of Technology
4800 Oak Grove Drive
Pasadena, CA 91109, USA

Tel: 818-354-8189 Fax: 818-393-6720
email: mrd@pacific.jpl.nasa.gov

Victoria I. Lytle

Antarctic CRC
University of Tasmania
GPO Box 252C
Hobart, TAS 7001
Australia

Tel : 61-02-207652 Fax: 61-02-207650
email : V.Lytle@antcrc.utas.edu.au

[†] (corresponding author)

Accepted for publication in: *Journal of Geophysical Research*

ERS-1 Radar and Field-Observed Characteristics of Autumn Freeze-up in the Weddell Sea

Mark R. Drinkwater
Jet Propulsion Laboratory
California Institute of Technology
4800 Oak Grove Drive
Pasadena, CA 91109
USA

Victoria Lytle
Antarctic CRC
University of Tasmania
P.O. Box 252c
Hobart, TAS 7001
Australia

Abstract

ERS-1 satellite microwave radar data are analyzed to investigate changes in sea-ice characteristics during a period when a drifting ice camp was deployed in the Weddell Sea, Antarctica. Synthetic Aperture Radar and scatterometer data are calibrated and geolocated to derive a time series of C-band backscatter coefficient (σ^0) corresponding with simultaneous surface measurements during the austral autumn freeze-up. Thermistor strings were implanted in the snow and ice at a number of local and regional sites. Surface measurements at these sites indicate that up to 50 % of the surface of ice floes surviving the summer were flooded, with an unconsolidated, saline slush layer at the snow/ice interface consisting of approximately half seawater and half ice of meteoric origin. The slush was typically 5 to 30 cm thick and covered by a 20 to 50 cm thick dry snow layer. Results show that the microwave radar backscatter characteristics of this perennial ice region responded sensitively to changes in air temperature and corresponding changes in turbulent flux of heat at the surface of the sea ice. At ice concentrations exceeding 95 %, the modulation of the regional backscatter coefficient by windspeed and direction was negligible. Warm summer conditions persisted for around two weeks after ice camp deployment on 7 February (day 38), with air temperatures of around -3 to -5° C prior to the onset of autumn freeze-up. From 26 February (day 57) onwards, cooling began and snow-ice growth proceeded as air temperatures fell to below -20° C. Altogether, between 7 February (day 38) and 15 March 1992 (day 75) the backscatter coefficient timeseries measured by each radar indicated that σ^0 fell by several dB's during the freezing and transformation of the layer of saturated, saline basal snow into snow-ice. This change is caused by a reduction in the permittivity and thus the scattering intensity of the basal snow as a function of the disappearance, by freezing, of the saltwater saturated layer. These results suggest the possibility of monitoring the timing and autumn freeze-up transition of regional ice signatures as a means of quantifying the proportion of flooded perennial sea ice.

Keywords: Synthetic Aperture Radar, Scatterometer, Weddell Sea, Antarctica, austral autumn, freeze-up, backscatter coefficient.

1.0 Introduction

The western Weddell Sea contains the largest proportion of the ice cover around Antarctica which survives the summer (~ 40 %), resulting in a large fraction of multi-year ice in the region. A snow cover as deep as one meter or more remains on top of the ice at the end of the summer. During the summer months, the temperature of the sea ice and the within overlying snow cover are close to, or at their melting point. With the onset of autumn, air temperatures drop, the basal snow and ice surface cools, and additional ice begins to form. The freezing process can have significant effects on the sea-ice biota, and the salt flux to the ocean [Fritsen *et al.*, 1994, Lytle and Ackley, 1996].

Ice convergence occurs in the western Weddell Sea as the ice is pushed against the Antarctic Peninsula [Drinkwater and Kottmeier, 1994]. Resulting compaction of the ice floes and dynamic thickening of the ice due to ridging, rafting and deformation creates a rough, deformed ice cover, with little open water. The small fractions of open water (usually less than 5 %) determine the extent to which the upper ocean communicates directly with the lower atmosphere, and regulate the magnitude of the ocean-atmosphere heat fluxes. This area of ice convergence and ridging also corresponds with a zonal maximum in annual precipitation [Eicken, *et al.*, 1994; 1995] along a swath between 70° and 75°S. Drifting snow rapidly accumulates around ridges and new ice in leads is quickly covered with snow. Thus, a combination of the higher albedo snow together with the shielding effect caused by its reduced thermal conductivity, and the low ocean heat fluxes, play an important role in ensuring the capability of this sea ice to survive the summer months. The annual drift of the ice is sufficient to advect most of this sea ice together with its accompanying snow cover out of the Weddell Sea within the next year, thereby representing a considerable annual flux of freshwater exported northward in the western branch of the Weddell Gyre.

During autumn, open water areas become regions of new ice growth and locations of high-rate brine production. The large fractions of old ice surviving the summer have a deep snow cover which insulates the ice surface and helps protect it from surface melting. This deep snow induces isostatic adjustment of the warm, permeable, basally melting summer ice, often resulting in flooding at the base of this snowcover [Lytle and Ackley, 1996]. The initial ice growth on these floes is primarily the formation of snow-ice as this flooded snow, or slush freezes, rather than congelation ice growth on the base of the floes. This additional component of snow-ice growth on the top of ice floes is thought to contribute as much as 10% to the net ice production in this part of the Western Weddell Sea [Eicken *et al.*, 1994], and furthermore, the convection occurring in the permeable isothermal ice cover can result in significant salt flux into the mixed layer beneath this multi-year ice cover [Lytle and Ackley, 1996].

To date, satellite microwave radiometers have been the only reliable source of frequent large-scale images of Southern Ocean sea-ice extent [Comiso *et al.*, 1992]. Passive microwave

instruments such as Electrically Scanning Microwave Radiometer (ESMR), Scanning Multichannel Microwave Radiometer (SMMR) [Gloersen *et al.*, 1992] and Special Sensor Microwave/Imager (SSM/I) [Cavalieri *et al.*, 1991] have been the primary source for synoptic historical data records describing ice extent and concentration in the Weddell Sea. These large-scale, low (25 km) resolution data are useful, however errors in the derivation of sea-ice concentration and ice type arise from the complexity of microwave emission and scattering from Antarctic sea ice at these frequencies, and because of the significant impact occurring from synoptic-scale meteorological systems [Oelke, 1996]. In particular, it is difficult to use these passive microwave data to quantify areal proportions of different ice types such as multi-year, first year, thin ice or open water. Algorithms that are used in the Arctic to identify multi-year ice are not applicable, largely because of the different physical processes which modify the emission and scattering characteristics of Antarctic multi-year ice.

In order to quantify perennial ice concentrations accurately, or to detail the ice deformation and distribution of open-water areas, a higher spatial resolution dataset is needed. Thus, a necessary complement to the daily, 25 km resolution, large-area mapping capability of the SSM/I instrument is high-resolution microwave radar. Until 1992, no such extensive radar dataset with supporting on-site data existed for sea ice in the Antarctic, and the only satellite-borne radar image data of the Weddell Sea was collected by the Shuttle Imaging Radar (SIR-B) in 1984 [Carsey *et al.*, 1986; Martin *et al.*, 1987]. The launch of the European Space Agency's (ESA) first European Remote Sensing Satellite (ERS-1) in July 1991 provided new observations of the Weddell Sea using a suite of microwave sensors including the Active Microwave Instrument (AMI) operating at C-band (5.3 GHz: 5.6 cm wavelength). For the purposes of this study, the AMI was operated either in an imaging, Synthetic Aperture Radar (SAR) mode, or non-imaging Wind Scatterometer mode by ESA [ESA Earthnet, 1992].

No long-term historical C-band surface scatterometer measurement archive is available for Antarctic sea ice, as currently exists from decades of surface-based Arctic studies. This made initial interpretations of Antarctic SAR images difficult, largely because of the lack of any historical or regional perspectives on the origins of backscatter variability [Drinkwater, 1995]. In this paper, we present a time series of ERS-1 SAR images taken over the same group of ice floes as they drift northward in the Weddell Gyre. These data were acquired in the region of the 1992 Ice Station Weddell (ISW) drifting ice camp experiment, where detailed meteorological, sea ice and snow data were collected on a routine basis. In addition, helicopter flights were periodically flown, and qualitative estimates were made of the regional sea-ice concentration and the amount of new ice forming in leads. We present a comparison of *in-situ* observations collected from ISW with the SAR and Scatterometer data and demonstrate that the C-band instrument is sensitive to the ice-surface changes occurring during the autumn freeze-up period. We find that SAR backscatter

signatures decrease during the onset of winter as the slushy snow, (occurring over 30 to 50 % of the surface area) freezes to form snow-ice. This decrease in the backscatter is opposite to the trend observed in the Arctic during the freeze-up period, where the backscatter from multi-year ice increases by 3 to 5 dB [Drinkwater and Carsey, 1991; Winebrenner *et al.*, 1996]. The recognition of this slush, and the timing of its subsequent freeze-up will help to monitor the freeze-up of the region and the onset of the salt flux into the ocean.

2.0 Ice Station Weddell

Ice Station Weddell (ISW) was deployed on perennial sea ice about 100 km from the ice edge in early February, 1992 at 71° 35' S, 50° 00.65'W. The camp drifted approximately 750 km northwards with the ice in the western limb of the Weddell Gyre [Gordon *et al.*, 1993] for four months before being recovered in June at 65° 38'S, 52° 25'W (Figure 1).

2.1 Camp Deployment, Drift and Recovery

Between 4 and 10 February 1992 the Russian icebreaker *Akademik Fedorov* deployed ISW and its personnel on an ice floe approximately 2.7 km x 1.7 km. The floe was comprised of a mixture of ice types ranging from 0.7 m thick, relatively undeformed ice, to 2 m highly-ridged ice. Figure 2a and 2b show portions of a SAR image of the region showing ISW, with the *Akademik Fedorov* in a lead next to the camp floe. Large-scale (*i.e.* metre-scale) roughness was characterized using the grazing-angle relative radar-scattering intensity (in fifths) from the shipborne radar on-board *Akademik Fedorov* (courtesy Valery Karpiy - AARI, and Steve Ackley - CRREL). This qualitative shaded scale of surface roughness in Figure 2c shows that the floe was comprised of ice with differing roughnesses characteristics as a result of differences in past deformation. In particular, there is a clear distinction between the northern portions of the floe which was relatively hummocked, and the smoother ice in the south. The smoother portion was later used as an airstrip for supply by ski-equipped Twin Otter airplane. This difference in roughness is apparent in the SAR image in Figure 2b, with the southern portion of the ice floe having a lower backscatter. Although field observations, and camp logistics considered these two portions a single floe, they have distinctly different backscatter values in the SAR image. This smoother region of the floe, although smooth on the decameter scale, still has a relatively higher backscatter than new ice which eventually formed in the surrounding leads.

2.2 Surface Measurement Sites

Frequently visited measurement sites were established locally and situated at distances of up to 2 km away from the camp (lettered; A, B, D, G, J, and V) on the camp floe (Figure 2c). A further

five remote sites shown in Figure 2d (named; Alex, Brent, Chris, Dimitri, and Ed) were also established between 20 and 100 km away from the camp [Ackley *et al.* 1992]. Routine helicopter flights were made to these locations, and observers estimated the amount of open water and new ice along the flight paths. Although their relative positions varied somewhat during the study period, particularly early in the experiment, two of the sites (Chris and Ed) remained approximately 50 and 100 km to the west. The other remote sites were 20 to 50 km to the south, east and northeast of the main camp.

2.2.1 Thermistor Strings

Thermistor strings were embedded in the ice and snow covers at all six local sites and at two of the remote sites, Chris and Dimitri [Lytle and Ackley, 1996]. Each location had different initial ice and snow conditions, with ice thicknesses ranging from 0.5 to 4.0 m and snow depths from 0 to 0.5 m. These required differing thermistor installations varying from 7 to 38 vertically distributed temperature measurements, with a vertical resolution of 5 to 20 cm, and a thermal accuracy of $\pm 0.03^\circ \text{C}$. Each of the thermistors initially extended from the air through the snow, slush and ice, and into the water, however at some sites the snow accumulation covered the thermistors completely. They were installed over a period of time from day 52 (site A) to day 67 (site J), and after installation temperatures were recorded hourly.

2.2.2 Meteorological measurements

A combination of sources are used to obtain a complete record of air temperatures and wind velocities. A Finnish Salargos buoy deployed on the remote floe Alex (Figure 2d), recorded hourly temperatures and winds [Launiainen and Vihma, 1994a; 1994b]. From day 57 onwards, routine hourly mean air temperature, wind speed, and direction were collected at ISW [Andreas *et al.*, 1992]. For the period of overlap, the air temperatures of the buoy and camp agree to within 2°C , and so the two data sets are compiled into a time series spanning the dates the SAR data were collected (Figure 3).

3.0 ERS-1 Satellite Radar Observations

3.1 ERS-1 Radar Data Acquisition

The European Research Satellite (ERS-1) SAR data acquisitions were restricted during the ISW drift by ESA's scheduling and to periods of data reception by the German Antarctic Receiving Station (GARS) on the tip of the Antarctic Peninsula (Figure 1). From day 38 to 74 (*i.e.* February 7 until March 14) the ERS-1 satellite was in a 3-day exact repeat orbit phase (known as the “Ice

Phase”) and was able to collect SAR data at the camp location [ESA Earthnet, 1992]. We use additional SAR data collected prior to the ice camp deployment on day 32 (February 1) to document ice conditions prior to camp deployment. Unfortunately, SAR data reception of the camp floe was not possible at GARS after day 74.

During periods when the SAR was not operating, the alternate low bit-rate wind Scatterometer (EScat) mode of the instrument enabled continuous measurement of radar backscatter coefficient ($\bar{\sigma}_{Scat}^{\circ}$) along a 500 km wide swath. We use both the high resolution SAR images, and the lower resolution EScat data in this study. The advantage of the EScat data is that they fill in periods in time in which no SAR data could be obtained, thereby providing a continuous backscatter record spanning the drift of ISW.

3.2 Temporal and Spatial Coverage

3.2.1 SAR Images

A total of 22 SAR image frames were collected over floes in the vicinity of the ISW camp between day 32 and day 74, 1992 (Table 1). Two SAR images were collected on day 32 to indicate initial conditions of the sea ice prior to ISW deployment (Appendix I). ISW drifted into the SAR imaging swath on day 38. Successive ascending orbit images of the ice camp and surrounding ice conditions were collected on days 38, 41 and 44 before ISW drifted northward into the cross-over location of two SAR imaging swaths on day 46. Between day 46 and 65, ISW remained within this cross-over location with successive images acquired on ascending and descending orbits (Figure 1). Between days 65 and 74 ISW drifted northwards into the ascending orbit swath only. Five further SAR images were collected on days 70, 71 and 74 before ISW drifted out of the ascending SAR imaging swath.

These SAR image data provide high-resolution (~25 m), all-weather day and night measurements of sea-ice backscatter ($\bar{\sigma}_{SAR}^{\circ}$) along a 100 km-wide swath at incidence angles of 20 to 26°. Resulting high resolution image frames described in Table 1 have dimensions of 100 x 102.5 km (range x azimuth) and an initial pixel spacing of 12.5 m. To reduce data volume and image speckle the data are spatially filtered using a block averaging procedure (reduced by a factor 1:8) and then geocoded in an SSM/I polar stereographic projection, with the plane at 70° S and reference meridian set to 0° W. Reduced resolution images are calibrated with a standard algorithm to obtain pixel backscatter coefficients [Laur, 1992]. The resulting confidence interval for the backscatter coefficient of a block-averaged image with 100 m pixel spacing, exceeds 90 % for a ± 1 dB error bound [Drinkwater, In Press]. For each entire image, a mean backscatter ($\bar{\sigma}_{SAR}^{\circ}$) was calculated by averaging all 100 m pixel values.

Multi-year ice backscatter

In addition to the global statistics from the SAR data, over 200 large, perennial ice floes are identified and their backscatter calculated over 2 to 15 SAR images. All floes were present after the peak in summer melt, and are therefore classified as multi-year floes. Tracking was achieved manually using an Interactive Data Language (IDLTM) image processing routine. Each floe was identified in an image, the outline of the floe drawn on the screen, and the size and average backscatter coefficient ($\bar{\sigma}_{MY}^{\circ}$) value calculated and recorded. The same floe was then identified in other images from different days, and the process repeated. To determine the accuracy of the method, several operators repeated the outlining of the floes: this resulted in a variation in the average backscatter of less than ± 0.5 dB. Floes varied in size from 0.4 km^2 to 60 km^2 with the average size about 6 km^2 , equivalent to the size of the main ice-camp floe. Due to the low contrast in the first images on February 1, explained in Section 4.3.1, we could not identify individual floes, and no floes are tracked from this date. Since the ice floes were advected first westward and then northward through the fixed orbit swaths, it was not possible to continuously track all the floes on all of the images.

3.2.2 Scatterometer Images

The periodic mesoscale SAR snapshots of ice conditions are supplemented using the EScat mode data from the ERS-1 AMI instrument. While ERS-1 SAR image pairs provide detailed indications of the ice motion and sea-ice conditions on the 100 km scale, time-integrated, medium-scale resolution, hemispheric coverage EScat images complement the SAR with uninterrupted mapping of basin-scale dynamics and the processes of the autumn advance of the entire sea ice cover [Drinkwater, In Press].

Enhanced resolution C-band backscatter images are produced from 500 km-swath, gridded EScat data, improving the intrinsic 50 km resolution to $\sim 20 \text{ km}$ [Drinkwater *et al.*, 1993; Long *et al.*, 1993] with a pixel spacing of $\sim 9 \text{ km}$ at 70°S . EScat images map the mean backscatter coefficient from a series of measurements at incidence angles in the range $20^{\circ} < \theta < 60^{\circ}$, for a given measurement cell location, according to the linear model;

$$\sigma^{\circ}(\theta) = \bar{\sigma}_{Scat}^{\circ} + M (\theta - 40^{\circ}). \quad (1)$$

Equation (1) provides a measure of the rate of change of backscatter coefficient σ° with incidence angle (θ) as gradient M [Drinkwater *et al.*, 1994], and a mean backscatter coefficient ($\bar{\sigma}_{Scat}^{\circ}$) normalized to 40° incidence (*i.e.* a higher incidence angle than the $20\text{-}26^{\circ}$ in SAR images). M

is found to be particularly sensitive to whether backscatter is caused by primarily surface or volume scattering [Drinkwater and Carsey, 1991].

Six-day EScat images of the entire Southern Ocean south of 55°S were generated throughout the 1992 winter (at 3-day intervals), to enable basin-wide Weddell Sea ice processes to be monitored [Drinkwater *et al.*, 1993]. These are used to obtain M and $\bar{\sigma}_{Scat}^{\circ}$ values [Drinkwater *et al.*, 1994] around the ISW location, as defined within the geographic bounds of the SAR image frames.

In summary, we use four different values to describe the sea-ice backscatter coefficient: $\bar{\sigma}_{SAR}^{\circ}$, (the global average of a SAR image), M and $\bar{\sigma}_{Scat}^{\circ}$, (the slope and the average backscatter at 40° incidence from the EScat images) and $\bar{\sigma}_{MY}^{\circ}$ (average backscatter of tracked multi-year floes within the SAR images).

4.0 Results

4.1 Meteorological Conditions

During ISW camp deployment, air temperatures ranged between -2 and -4° C and remained below freezing for the rest of the experiment. Air temperatures in Figure 3 can be roughly divided into two different time periods. Prior to day 57, temperatures were generally warmer than -8° C. The only exceptions to this were days 47 and 50, when temperatures reached as low as -15° C for two or three hours. After day 57, except for a short warm period from day 62 to day 64, temperatures steadily decreased and remained between -15 and -25° C for the remainder of this study.

Low pressure and accompanying strong southwesterly winds at the outset of the drift generally exceeded a mean value of 5 ms⁻¹ from day 35 to 47. A brief period of easterly winds in the period between day 53 and 57 advected warm air over ISW before the wind direction veered back to southerly and cooling set in. With relatively higher pressure and stable conditions wind speeds remained around 3 ms⁻¹, with the exception of one stormy period between day 64 and 66 during a cold air outbreak from the south, when wind speeds exceeded 10 ms⁻¹. Wind speeds and air temperatures at the SAR imaging times are listed in Table 1.

4.2 Snow and Sea-Ice Conditions

4.2.1 Ship Observations Prior to and During ISW Deployment

Ice observations were collected by observers aboard the *Akademik Federov* as it traveled to the ISW deployment location. These were collected hourly while the ship was underway, using the method described by Allison and Worby (1994). Ice concentrations exceeded 80 % after passing

south of the location 70.4°S, 50.1°W early on day 34. At this location, the ice concentration increased significantly, during transit through a band of highly deformed old ice reaching an average thickness of as much as 3 m. After this band, the ice concentrations remained greater than 80 %, with more thinner (30-40 cm) ice. Openings between ice floes were generally wide (> 50 m), and the ship made good progress following leads, generally travelling at speeds in excess of 3 ms⁻¹ (6 kt). Prior to reaching the final camp location, the concentration of thicker, highly deformed floes decreased to about 10 %, and the remaining floes (80 %) were about 50 to 60 cm thick, with a snow layer which was flooded in some locations. Immediately around the camp, the ice concentration was 80% to 90%, with new grease ice beginning to form in the leads.

4.2.2 Sea-Ice and Snow Conditions at ISW

After the camp was fully established on day 46 (February 15), snow and ice physical properties were routinely measured at the surface measurement sites.

Snow Pits

Snow pits were periodically dug in the vicinity of the thermistor strings, and snow characteristics such as the temperature, density, salinity and grain size were measured. A total of 12 snow pits are used for this study. Three snow pits each were dug at sites A and B from day 55 to day 67, one additional snow pit was examined at site A on day 89, two weeks after the final SAR overpass. One snow pit each was dug at sites D and G and at three of the remote sites (Chris, Dimitri and Ed). Sites V and J initially had no snow cover, although both subsequently had snow accumulation.

Snow pit depths varied from 10 cm on newly frozen lead ice at remote site Chris, to 58 cm at site A, a deformed ice site close to the ice camp (Figure 2). Samples of known volume were collected at vertical intervals within the snow pit, and weighed to calculate a density. These samples were then melted and the salinity of the meltwater measured. The salinity was 0.0 psu (*i.e.* practical salinity units) in all samples in 8 of the 12 snow pits. In one pit, the salinity at the base of the snow was 1.7 psu. In 3 of the pits, the upper portion of the snow had no salinity, but a saturated basal slush layer was discovered. In these cases the slush was about 50:50 water and ice (or snow), and the bulk salinity varied from 15 to 17 psu. Just above this slush, a 5 cm layer of snow had salinities ranging from 0.2 psu to 1.7 psu.

At site A, a highly deformed region, this slush layer was found in one of the two snow pits examined on day 55. At site B, an undeformed site, the layer was continuous and found in snow pits dug on day 55 and day 67. In all cases, this slush layer was overlain by dry snow, and there was no visible sign of the flooding from the surface. This slush had formed either by infiltration of sea water from the sides of the floe, or vertically through the permeable ice [Fritsen *et al.*, 1994].

Although there may have been some melt water from the snow included in this slush, the high salinity and the location of the top of the slush layer near sea level indicate it was primarily caused by sea water infiltration. Further biological and salinity data [Fritsen *et al.*, 1994] confirmed that this slush layer was hydraulically linked to the underlying ocean.

Temperatures were measured at 2.5 cm vertical intervals in the snow pit, and agreed well with the more continuous (in time) data obtained from the thermistor strings. On day 55, snow temperatures were near isothermal, and ranged from -1.1°C to -1.8°C . As air temperatures decreased, the snow pack cooled from the surface downwards, and by day 70, the ice-surface temperature at all sites was less than -2°C [Lytle and Ackley, 1996]. At sites with thinner snow cover, this cooling occurred much sooner. At site A, the initial ice thickness was 1.1 m with a snow layer 0.4 m deep, and a basal slush layer varying between 0 and 0.13 m thick. The snow layer was initially isothermal at around -1°C . By day 70 the slush layer had completely frozen downward to the sea-ice surface.

Early in the experiment, snow densities varied from 260 kgm^{-3} to 470 kgm^{-3} with the density increasing with depth in the snow. The snow was generally fine grained (diameter less than 0.5 mm), and three of the deeper (0.39 to 0.58m) snow pits had ice layers within the snow, indicating previous melt episodes. Later, on day 73, lower density snow (190 kgm^{-3}) was observed near the base of a 25 cm snow pit, within which a 4 to 5 cm thick layer of depth hoar crystals had developed. These crystals were several millimeters in diameter and were found in increasing amounts in the snow pits as the cold air temperatures persisted. We did not find ice layers within the snow cover, although some of the snow was very hard, particularly near the base of the snowpack. It was difficult to collect density samples because the cutters would not penetrate, however where we could sample it the density was still about 450 kg/m^3 . These hard layers were probably formed by refreezing of wet snow.

Drilled holes

During ISW deployment, for logistics requirements, 57 holes were drilled at random locations on the floe. The snow and ice thickness measured and the presence of a basal slush layer was noted. Ice thickness varied from 0.78 m to greater than 3.4m, with an average of 1.5m. The snow depth ranged from 0.14 m to 0.75 m, with an average of 0.4 m. Half of these random locations had a slush layer at the base of the snow.

Snow and ice thicknesses were measured at one meter intervals along a 100 m profile line near site A [Lytle and Ackley 1996]. On day 56, 80% of the holes had an ice surface below sea level, and slush at the base of the snow. Some of this slush was quite thick, and the average ice elevation was 0.12 m below sea level. This line was re-surveyed on day 112, after much of the

slush had frozen, creating snow-ice; only 34% of the ice was below sea level and the average ice elevation was 0.04 m above sea level.

Ice Cores

Ice cores were collected periodically, and analyzed for salinity and ice structure. The top 5 cm of the ice had salinities which were generally greater than 5 psu, and often as high as 15 or 20 psu. The snow cover insulated the ice, which during the study period (until day 74) remained warmer than about -5°C . Exceptions to this occurred only in ridged areas where the snow had been scoured, and the ice surface was exposed to cold air temperatures. This combination of warm, porous and relatively salty ice resulted in considerable liquid brine at the ice surface. Consequently, we estimate little or negligible penetration of the microwaves into the ice surface, with the majority of the scattering occurring from the snow cover, or the surface of the ice or slush.

Summary of snow conditions

The snow cover in the region was variable in depth, ranging from no snow on the tops of ridges and on newly formed leads, to over 0.7 m where the snow had collected in the lee of ridges. From the random drilling locations, and the profile lines we estimate that from 30% to 50% by area of the ice initially had a slush layer at the snow/ice interface caused by intrusion of sea water into the snow by early February. In deformed areas of ice, this slush layer was discontinuous; a thick (up to 0.3 m) layer of slush could occur in the lee of ridges, with a completely dry snow cover within several meters near the top of the ridges. In undeformed regions the slush layer was more spatially uniform and the snow would either be completely dry (no slush), or have a continuous slush layer over tens of meters (*e.g.* site B). In all cases we found that snow above about 10 cm above the slush was dry, and contained no salt. By day 70, this slush had frozen creating snow-ice [Lytle and Ackley 1996] and had an identical crystal structure, and salinity which was indistinguishable from the underlying granular ice. After this time, wet snow was found only near newly formed ridges and because of the cold air temperatures the froze quickly (less than one day).

As air temperatures dropped, the vertical temperature gradient in the snow pack increased. This enabled formation of large, depth hoar crystals near the base of the snow, by the mechanism of temperature-gradient metamorphism [Sommerfeld and LaChapelle 1970].

4.2.3 Helicopter Site Sampling

Helicopter flights were made once or twice a week as logistics and weather permitted. During these flights, observers on board estimated the amount of open water, new, nilas and thicker, snow-covered ice (Table 2). Because we flew to the same remote sites, the same general collection of floes were overflown each time a flight went to a specific remote site. With the exception of the last

flight on day 74, the estimates were made by the same observer. These are quantitative estimates and the errors are difficult to assess. For days where the open water is listed as zero, no open water was observed during the flight. At ice concentrations ranging from 1 to 10%, the errors are estimated to be less than 4 %. For higher concentrations the errors are estimated to be less than 10 %. Early conditions on day 43 indicated 10 to 20% open water to the east of the camp. On the day 48 flight to the south and east of the main camp, we observed about 3 % open water, and 3 % new ice around the camp and after this time, there was less than 8 % open water, and on four flights, no open water was observed.

Based on the observations both from the air, and from the ship, there was a significant decrease in open water fraction between day 32 (just after the initial SAR data were collected) and day 48. Rather than additional new ice growth, this was primarily the result of compaction of the ice in the region. This is confirmed by helicopter observations where new ridging was observed around the edges of floes. The relative GPS locations of the remote sites also confirm this deformation activity. For instance, site Alex deployed about 50 km due east of the ice camp floe on day 37, had moved slightly south relative to the main ice camp floe, and was about 45 km away. After day 43, site Alex moved south and west (relative to the ISW-camp floe), and was only 24 km away at a heading of 150° (south east) on day 48 (see Figure 2d). This period also corresponds to an increase in the velocity of the overall pack, and a change in the drift direction [Drinkwater and Kottmeier, 1994]. After this time, we continued to observe new ice formation (up to 20%), but there was no large scale relative movement of the remote floes.

4.3 ERS-1 Radar Observations

4.3.1 Calibrated Sea-Ice Backscatter Characteristics

Comparisons of histograms of calibrated SAR backscatter coefficient (derived from all pixel values an entire SAR image) are a useful indicator of changes occurring in response to variations in the regional sea-ice characteristics. Backscatter coefficient distributions represent mixtures of backscattering from snow-covered multi-year ice, new or first-year ice, and open water found in the region. Such SAR image backscatter histograms are presented in Figure 4 for; (1) day 38 at ice camp deployment; (2) day 41; (3) day 70; and (4) day 74 (see Appendix I). These four dates were selected by using the meteorological record from ISW (in Figure 3) to subdivide the SAR imaging window into periods with markedly different temperatures or wind speeds, before and after freeze-up. The first two dates represent the early, relatively warm phase of the experiment. For histogram 1 ($\bar{\sigma}_{SAR}^{\circ} = -8.0$ dB), windspeeds exceeded 9 ms^{-1} with an air temperature of -2.8° C ; and for histogram 2 ($\bar{\sigma}_{SAR}^{\circ} = -7.97$ dB) the windspeed remained 8.7 ms^{-1} but the air temperature dropped slightly to -6.9° C . Colder conditions, with air temperatures below -19.0° C , are represented by the

latter two dates. For histogram 3 ($\bar{\sigma}_{SAR}^{\circ} = -8.9$ dB), winds were calm at 2.6 ms^{-1} , and for histogram 4 ($\bar{\sigma}_{SAR}^{\circ} = -9.6$ dB) increased again slightly to 4.2 ms^{-1} .

In histogram 1 in Figure 4, the relatively high wind speeds and air temperature ensured that the snow cover was near isothermal. The SAR image has a small range of relatively high backscatter values (between -10 and -5 dB). A lack of contrast between ice floes and the surrounding matrix of wind-roughened open water, makes it difficult to identify individual ice floes. *In-situ* data collected upon arrival indicated that the snowpack was warm, and had previously contained some liquid water. Thus, the scattering mechanism causing a mean of -8.0 dB and modal value of -7 dB is predominantly surface scattering. Scattering occurs primarily from the slush/snow interface where it is present, from the ice/snow interface in areas where there was no flooding and little snow liquid water, or from the snow surface if liquid water was present. Values below -10 dB indicate smooth first-year ice or nilas-covered leads, while the small tail at values exceeding -5 dB is caused by bright, wind-roughened leads in this image.

Histogram 2 in Figure 4 (three days later), shows a large change in the backscatter coefficient distribution for a case where the temperature drops and the winds remain relatively brisk. *In situ* observations show that the temperature of the snow cover was just below freezing, and that the upper layers of the snow were dry. With less attenuation through the snow cover, the scattering surface (ice or slush) of the multi-year ice floes becomes a more effective scatterer and the mode in the histogram increases to -6 dB. The most dramatic change is the increase in the contrast between the multi-year ice floes and the leads. The unimodal distribution begins to bifurcate into an overlapping bimodal distribution with a noticeable bulge developing at lower backscatter pixel values. This bulge at values below -9 dB and the tail extending to values below -15 dB represents first-year ice, nilas and calm open water in the SAR image.

Histogram 3 (day 70) shows a case after the onset of freeze-up, with calm winds and a mean air temperature of -19.3° C . Thermistor data indicated that the cold wave had already penetrated beyond base of the snow, and that the slush at the snow/ice interface had frozen into snow-ice (*i.e.* a mixture of meteoric ice and seawater). SAR images indicate that the backscatter coefficient of multiyear floes has changed considerably, as indicated by the reduction in the mode in the histogram around -8 dB. New lead ice formation also causes the low-end values in the distribution to drop below -15 dB.

With the continuing freeze-up, by day 74 all remaining open leads became frozen. Histogram 4 has a lower mean value of -9.6 dB, and a mode at -8.5 dB. The decrease in multi-year ice backscatter has reduced the high-end values to below -5 dB. The lower end of the distribution is similar to day 70, (histogram 3) as new ice continues to form and thicken in the leads.

4.3.2 SAR-derived Sea-Ice Concentration

Wind blowing on the surface of open leads can exert a significant influence on the global SAR backscatter coefficient. At ice concentrations less than 100%, wind-roughened capillary waves on open leads are a common source of extremely bright pixel values (approximately -5 dB at wind speeds of 5 - 6 ms⁻¹ as derived using the CMOD4 algorithm [Stoffelan and Anderson, 1993]). Measurements of the amount of ice divergence or changes in the mesoscale characteristics of the ice pack are therefore essential to corroborating that $\bar{\sigma}_{SAR}^o$ changes are independent of mesoscale ice conditions or indeed the fraction of wind-roughened open water. Estimates of sea-ice concentration and of the areal coverage of leads were made from classified SAR images with the results are indicated in Table 1. Images were first automatically classified using simplified decision-rule based class boundaries, defined by the following backscatter ranges in the calibrated SAR images [Drinkwater and Haas, 1994; Drinkwater *et al.*, 1995];

Nilas:	$-25.5 \text{ dB} \leq \bar{\sigma}_{SAR}^o \leq -22.5 \text{ dB}$
Open Water:	$-25.5 \text{ dB} \leq \bar{\sigma}_{SAR}^o \leq -20.5 \text{ dB}$ (Calm) $-4.50 \text{ dB} \leq \bar{\sigma}_{SAR}^o \leq -1.50 \text{ dB}$ (Windy)
First-year ice:	$-20.5 \text{ dB} \leq \bar{\sigma}_{SAR}^o \leq -10.5 \text{ dB}$
Multi-year ice:	$-10.5 \text{ dB} \leq \bar{\sigma}_{SAR}^o \leq -4.50 \text{ dB}$
Icebergs:	$-1.50 \text{ dB} \leq \bar{\sigma}_{SAR}^o \leq 0.00 \text{ dB}$.

Class boundaries were then manually adjusted, based on *a-priori* information (*i.e.* temperature, wind, and ice motion/deformation conditions) and matching of known ice conditions local to ISW. On the 100 km scale, the resulting SAR-derived ice concentrations vary between 91 % and 99 %, agreeing closely with the regional observations from the helicopter (Table 2). Generally, ice concentrations varied around 95 %, with typically 80 % comprising multi-year ice floes. From these data, changes in $\bar{\sigma}_{SAR}^o$ were found to be uncorrelated with changes in the regional ice concentration or indeed the co-occurrence of high windspeeds and relatively larger open water fractions.

4.3.3 Modulation of Radar Backscatter by Wind and Temperature

In order to further rule out effects of wind we investigated the relationship between $\bar{\sigma}_{SAR}^o$, $\bar{\sigma}_{Scat}^o$, and the mean regional wind and temperature conditions. Because of the relatively small amount of open water in the region, we expect negligible influence of the wind on the global backscatter values. The temporal evolution of $\bar{\sigma}_{SAR}^o$ and $\bar{\sigma}_{Scat}^o$ is shown in Figure 5a. Despite winds

varying from 2 to 9 ms⁻¹ there is no correlation between the wind speed and $\bar{\sigma}_{SAR}^\circ$ or $\bar{\sigma}_{Scat}^\circ$. Each signature trajectory is similar in its characteristics, and the effect of the wind on the backscatter values is negligible over the first 15 days. The peak in wind speeds at day 64 (in Figure 3) is shown as a sudden diversion (marked by a circle) in both trajectories in Figure 5a. A large increase in $\bar{\sigma}_{SAR}^\circ$ is anticipated during such a wind-burst, if leads are an important contributor to the global backscatter values. In contrast, backscatter values actually fell at both 23° and 40° incidence during this event, due to enhanced ice formation in the leads.

Correlations between air temperature and backscatter are shown in Figure 5b. As air temperatures decrease from near freezing to below -20°C there is a decline of almost 2 dB in both $\bar{\sigma}_{SAR}^\circ$ and $\bar{\sigma}_{Scat}^\circ$. Linear regression coefficients of $R = 0.85$ and 0.90 are found for the SAR and EScat backscatter coefficient data, respectively.

5.0 Discussion

Combined SAR and EScat datasets allow compilation of a time-series of radar backscatter over the period coinciding with ISW surface measurements. SAR images represent a “snap-shot” of ice conditions on a particular day while EScat image data indicate the mean values for a 6-day window centered upon the day of interest, for any given SAR image (Appendix I). Onset of autumn freeze-up is captured well by the merged radar backscatter timeseries. Backscatter signature changes are explained and quantified first in terms of the thermodynamic changes which drive them, and then contrasts are drawn with the typical Arctic freeze-up scenario. To conclude, we present a heuristic model which describes the autumn freeze-up transition in the Antarctic, together with a characterization of the physical changes occurring in the snow and ice characteristics.

5.1 Summer-Autumn C-band Radar Backscatter Transition

Variations in the mean backscatter coefficient of multi-year ice floes, $\bar{\sigma}_{MY}^\circ$, global SAR image mean backscatter coefficient, $\bar{\sigma}_{SAR}^\circ$, and corresponding EScat values, $\bar{\sigma}_{Scat}^\circ$ and M are shown in the timeseries in Figure 6. Error bars indicated for $\bar{\sigma}_{MY}^\circ$ data points represent the range of mean values observed for tracked multi-year ice floes. $\bar{\sigma}_{SAR}^\circ$ varied between -6.8 and -7.7 dB until after day 64 when it decreased almost 2 dB to vary from -8.5 to -9.3 dB. The peak values in $\bar{\sigma}_{SAR}^\circ$ and $\bar{\sigma}_{MY}^\circ$ occurred on day 46 when air temperatures briefly warmed up. $\bar{\sigma}_{MY}^\circ$ has a trend similar to that of $\bar{\sigma}_{SAR}^\circ$, but because it doesn't integrate lower backscatter returns from small concentrations of thin and first-year ice it is generally 1 to 2 dB higher. $\bar{\sigma}_{MY}^\circ$ varied from -5.1 to -6.3 dB until day 64,

and then decreased to between -7.0 and -7.9 dB. Prior to day 64, the individual multi-year ice floe backscatter values varied between -4.1 and -7.5 dB, probably due to their different snow and surface roughness characteristics. However, they all showed a similar decrease of about 1.8 dB between day 64 and day 72. At the end of our time series, multi-year ice floes continued to have the highest $\bar{\sigma}_{SAR}^{\circ}$ values (aside from the icebergs), in the range -4.8 to -9.6 dB.

$\bar{\sigma}_{Scat}^{\circ}$, is 3 to 5 dB less than either $\bar{\sigma}_{SAR}^{\circ}$ or $\bar{\sigma}_{SY}^{\circ}$ because of its greater incidence angle at the surface. It shows a similar trend of decreasing values, although the decrease occurred earlier, possibly because it is integrated over several days. $\bar{\sigma}_{Scat}^{\circ}$ varied from -10.1 to -11.3 dB until day 62, and then decreased to between -11.6 and -12.3 dB. The gradient M decreased steadily from 0.22 on day 38 to 0.16 dB/deg by day 53, then increased again to 0.20 dB/deg by day 62. It then showed a sudden large drop to its lowest value of 0.13 dB/deg on day 64, before increasing slightly to values around 0.16 dB/deg by the end of the timeseries.

The decrease in the mean backscatter $\bar{\sigma}_{MY}^{\circ}$ occurred at the same time as the decrease in $\bar{\sigma}_{SAR}^{\circ}$ implying that perennial ice-floe signature variations are responsible for the large-scale regional backscatter signature variations. *In-situ* observations show that about 80 % of the ice consisted of multi-year floes, and thus it is expected that changes in $\bar{\sigma}_{MY}^{\circ}$ result in similar changes to $\bar{\sigma}_{SAR}^{\circ}$. They also indicate that the decrease in $\bar{\sigma}_{SAR}^{\circ}$ is not caused by the progressive formation of new ice types, such as nilas and first-year ice with lower backscatter values, but rather a change in the backscatter coefficient of the multi-year floes themselves.

Because the scatterometer data are six-day moving averages (each centered on the day of interest), they act as an integrator over time, thereby sensing any changes occurring slightly before or after the snap-shot time of individual SAR image frames. At times when there is a deficit of SAR information, such as the period when the major changes begin to occur in the slush layer (*i.e.* after day 64), the scatterometer values help fill in the data gap. The earlier decrease in $\bar{\sigma}_{Scat}^{\circ}$ relative to the drop in $\bar{\sigma}_{SAR}^{\circ}$ and $\bar{\sigma}_{MY}^{\circ}$ indicates that the change in backscatter occurred closer to day 64 than to day 70 (after the freeze-up), when the next SAR image was collected.

The timing of these decreases in backscatter (in Figure 6) correspond to a period of significant changes in the physical properties of the ice and snow cover. On day 64, the air temperature dropped steeply, increasing temperature gradients within the snow pack from around 0.2 C/m to as much as 0.7 C/m (Figure 6b). By day 60 the top of the slush layer at site A had cooled to -1.8° C and this layer began to freeze, as illustrated in Figure 7. The freezing isotherm (-1.8° C) moved slowly downward from the top of the local slush layer (around +10 cm above sea level) on day 60 to the original ice surface on around day 68 (indicated by triangle), reaching -10.0

cm beneath the original sea-ice surface by day 75. During this period the liquid water content of the layer had decreased from around 50 % to less than 5 % [Fritsen *et al.*, 1994].

5.2 Thermodynamics of Autumn Freeze-up

On the basis of the radar backscatter trends and field-observed snow and ice characteristics, a heuristic model is developed in this section. The schematic diagram in Figure 8 is used to describe and characterize the primary changes taking place in this location during austral freeze-up.

5.2.1 Implications of Flooding

Flooding at the base of the snow cover, and the subsequent freezing of this slush layer has significant thermodynamic and biological implications [Fritsen *et al.*, 1994; Lytle and Ackley, 1996] in addition to having a considerable impact on the C-band radar measurements. The snow-ice formed by this process during autumn freeze-up also comprises a significant portion of the pack ice. Lange *et al.* (1990) and Eicken *et al.* (1994), for instance, estimate that around 4 - 7 % of the sea ice in the Weddell Sea is composed of snow-ice. In concurrence with this observation, our measurements appear to indicate that this ice formation process is widespread in this region at the end of summer.

The schematic ice characteristics changes in Figure 8 indicate that the deep snow cover, observed on thick sea ice at the end of spring, provides the insulation required to protect the ice from melting during the summer months (in phase I). Beneath this layer of snow, the sea ice becomes isothermal at temperatures approaching the melting point. Ice floes respond isostatically to either bottom melting (positive) or additional snow loading (negative) by precipitation (each marked by upward or downward facing triangles, respectively). The warm sea ice becomes porous and a well developed brine-channel network develops (phase II). This network is proposed as the conduit by which undeformed ice floes may become flooded. The ice may also be flooded near regions of deformation, but this is more likely flooding occurring from depressed edges of the floe. Figure 8 shows that as the freeboard of an arbitrary ice floe adjusts to increased loading or bottom melt and reduced buoyancy, the sea-ice surface is depressed beneath sea level. This results in brine flowing upwards through the brine channel network onto the surface of the ice, thereby saturating the basal snow. The flooding process fills in any low regions of the ice floes, and this slush layer smooths out the large scale (decimeter) ice-surface roughness. Centimeter scale roughness created by the snow grains, on the surface of the slush remains to provide an effective scattering surface at C-Band. The brine/ice mixture remains at a constant freezing temperature regulated by its salinity, and until the slush layer freezes (in phase III) the underlying ice remains isothermal. The rate at which the slush layer freezes is dependent on the snow depth and the air temperature.

5.2.2 Physical Mechanisms

Early in the timeseries of radar data, prior to ISW deployment, backscatter values were depressed from their peak value on day 46 ($\bar{\sigma}_{SAR}^{\circ} = -8.02$ dB and $\bar{\sigma}_{Scat}^{\circ} = -11.3$ dB, respectively). The observation of distinctive icy layers within some of the snow pits (described in section 4.2.2) indicates that some liquid water existed in the upper snow pack prior to ISW deployment. It is speculated that snow melt is responsible for the uniform texture and lower σ° of the ice pack in the initial SAR backscatter image pair on day 32 (Appendix I). We have no *in-situ* data to confirm this, but as the air temperatures fell from their seasonal maximum, it is suggested that any liquid water froze within the snow pack to form the observed layers. By early February and the first snow pit samples, there was no liquid water remaining in the upper portion of the snowpack.

In general, the high ice surface salinity (and corresponding high brine volume) result in little radar signal penetration into the ice. Consequently, the primary surface scattering is expected to be from the snow/ice or the slush/snow interface, in addition to possible volume scatter from the snow.

Because the slush layer is initially about 50% water, and then froze, the upper surface of the slush layer, (or after freeze-up the surface of the ice), is the primary source of electromagnetic scattering. Because the snow cover was dry above the slush layer, we assume that surface scatter from the slush/snow interface, or ice/snow interface, was the primary scattering mechanism. Surface scatter as the primary scatter mechanism is supported by higher M values found early in the experiment (Figure 6c). As the slush layer froze, its dielectric constant, and hence the magnitude of the surface scattering changed. Although the cm-scale surface roughness of the slush may have also changed during freeze-up, here we show that the change in dielectric constant alone is sufficient to explain the observed change in backscatter. This idea is supported by independent C-band measurements of slush on first-year ice elsewhere in the Weddell Sea [Hosseinmostafa *et al.*, 1995; Lytle *et al.*, 1996].

For surface scattering models, the magnitude of the scattering is directly proportional to the power reflection coefficient. Because the snow-ice formed from freezing of this slush layer has significantly less liquid brine than the original slush layer, it also has a considerably different dielectric constant, and hence reflection coefficient. The slush initially comprised a mixture of ice crystals and brine, in approximately equal proportions. The brine in this mixture had a salinity of between 30 and 35 psu (i.e. similar to the original seawater), and therefore the bulk salinity of the slush mixture (when melted) was 16 to 18 psu. When freeze-up occurs, the complex dielectric constant of this slush changes from a value of $\epsilon^* = 20.0 - j11.0$, corresponding to a 1:1 mixture of brine and pure ice crystals (where the value for seawater at freezing point is $\epsilon^* = 55.0 - j41.0$), to

permittivity values more typical of sea ice ($\epsilon^* = 4.25 - j0.1$) [Hallikainen and Winebrenner, 1992] of around 6 psu bulk salinity [Lytle and Ackley, 1996]. For an average snow density of 300 kg m^{-3} the dielectric constant is about 1.4 [Glenn and Paren, 1975]. Using these values, the calculated magnitude of power reflection coefficient as the slush freezes, is reduced from 0.78 to 0.07, and equivalent to a decrease of 10 dB at normal incidence for a plane reflector. While these are only general estimates of the dielectric constants and resulting reflection coefficients, our observations together with model simulations by Lytle *et al.* (1996) demonstrate that the freezing of this slush layer is sufficient to cause a large change the backscatter, simply by changing the dielectric constant. The difference between the 10 dB estimated decrease in reflection coefficient, and our observed 2 to 3 dB decrease is due at least in part to the fact that the floes were not completely flooded, and the fact that the competing effect of hoar frost development tends to counterbalance the reduction due to salinity changes.

The maximum backscatter values on day 46, corresponding with slightly warmer temperatures, suggest a stronger contribution from snow-surface backscattering as the snow surface warmed. The lack of significant associated change in $\bar{\sigma}_{Scatt}^o$ or M , which are averaged over 1 week suggests that this change was short lived. Subsequently, M followed the snow-temperature gradient extremely closely. The large decrease in M on day 64, and the subsequent lower values are an indication of an increase in volume scatter at 40° incidence. Day 64 corresponds to the beginning of the formation of large depth hoar crystals (3-4 mm in diameter) as discussed in section 4.2.2 which may be the source of this volume scatter. The negative correlation between M and the snow temperature gradients is consistent with the argument that snow volume scattering contributes to regulating signature characteristics. It is difficult to quantify the areal extent of the depth hoar, but the large air temperature decrease around day 64, causing a large increase in temperature gradient in most of the snow pack will produce the conditions required for its formation over most of the region. Consequently, although the ice/snow interface continues to be the primary scatterer, depth hoar formation within the snow from day 64 onwards, and the decrease in M values are consistent with a combination of snow volume scattering and rough surface scattering from the snow-ice interface.

5.3 Contrast between Antarctic and Arctic C-band Autumn Observations

These results show a dramatically different progression from summer to autumn conditions than is typically observed in the Arctic [Drinkwater and Carsey, 1991; Gogineni *et al.*, 1992; Winebrenner *et al.*, 1996]. Whereas during the course of autumn freeze-up, C-band Arctic multiyear ice signatures increase from a summer minimum of around -13 dB to a maximum of around -10 dB, our Antarctic cases mirror the trend with opposite sense. This unanticipated result highlights the

importance of physical differences between perennial ice in each hemisphere at the end of the summer, together with the thermodynamic changes occurring during this seasonal transition period. A deep snowcover survives throughout the summer on perennial Antarctic ice [Massom *et al.*, 1997] in contrast in the Arctic, snow is typically either completely removed from ice floes by summer ablation, or partially metamorphosed into a superimposed ice layer. Radiational heating and cooling during diurnal cycles, and drainage of free-liquid melt water into well-defined pools together result in a hummocked and meltponded Arctic multi-year ice surface topography. Snow melt, flushing and brine drainage produces a relatively low surface salinity layer (containing voids and air bubbles in raised portions of the floe) which has no equivalent in the Antarctic perennial ice zone at the end of summer. As autumn freeze-up occurs and fresh-water melt ponds refreeze and disappear, bubbles within the cold, desalinated snow-ice, together with the air-ice interface, become the primary scattering source [Drinkwater and Carsey, 1991; Gogineni *et al.*, 1992]. This results in an Arctic multiyear microwave signature characterised by volume scattering [Hallikainen and Winebrenner, 1992], which displays little variation with incidence angle and has typical linear gradients of $M = 0.125$ dB/deg in the range $20^\circ < \theta < 60^\circ$.

In this study, we identified large, snow-covered multi-year floes with an average backscatter of -6.3 dB, almost 4 dB higher than the -10.2 ± 1.01 dB observed for winter Arctic multi-year ice floes [Fetterer *et al.*, 1994] and also greater than the anomalously high -8 dB value reported by Winebrenner *et al.* (1994) for cold, winter multi-year ice. Due to high surface salinity of the ice or saturated basal snow in this region (and thus high microwave absorption coefficient), internal volume scattering from inhomogeneities (such as bubbles) within the sea ice plays a negligible role in backscattering. Evidence provided by the range of floe backscatter measurements, as indicated as bars on $\bar{\sigma}_{sy}^o$ in Figure 6c, and the non-uniform nature of backscattering from the ice floes (in Figure 2) support the assertion that the signatures between days 32 - 46 result from primarily rough surface scattering (i.e. from the slush/snow, or ice/snow interface), yielding values of $M = 0.2 - 0.22$ dB/°.

6.0 Conclusions

Variations in backscatter of sea ice are investigated at a variety of spatial scales from individual floes to 100 km during the period of the drift of ISW, to determine whether the austral autumn freeze-up drives measurable changes in radar backscatter values measured from space. At the end of the freeze-up period there are significant differences between the newly formed ice in leads and multi-year ice floes; the latter have an average backscatter of -9 dB, while the new ice is -15 dB, or lower.

Backscatter from summer Antarctic multi-year ice is equal to or greater in magnitude than typical midwinter Arctic, multi-year ice. However, it is unlikely that volume scatter contributes any significant part of Antarctic sea-ice backscatter, due to the high brine content in basal snow at the ice surface, and the lack of air pockets. Rather, the observed trend is predominantly the result of surface scattering initially from the snow/slush (or snow/ice interface where there is no slush layer), which at the outset was estimated to cover 30-50 % of the region. As this slush layer freezes, and the amount of liquid water decreases from an estimated 50 % by volume to 5 % by volume, the reflection coefficient decreases by an order of magnitude. This new sea-ice surface, of lower reflectivity than the original slush layer therefore causes an overall decrease in the backscatter of 1-2 dB. Since a significant temperature gradient exists in the snow pack, depth hoar formation is encouraged, and although volume scatter increases the surface scatter is still the dominant mechanism.

As C-band radar penetrates through the dry summer snow at the surface of Antarctic ice floes, remote sensing techniques using ERS-1 radar data are an effective tool with which to study the timing of snow-ice formation in this and other similar sea-ice regions, and to use as a proxy indicator of algal growth within the ice pack. Based on precipitation patterns, the prevalence of perennial ice, and preliminary observations of similar trends in the microwave time-series, the mechanism of snow-ice formation is also anticipated to be particularly widespread in the Bellingshausen and Amundsen Seas, where extreme snow loading has been observed in the field. Evidence for upward accretion of meteoric ice [Kawamura *et al.*, In Press] has also been found for instance in Lützow-Holm Bay, in the region offshore from the Japanese Syowa station.

Future work combining ice-floe tracking technology with the radar signature tracking capability will improve characterization of the seasonal transitions undergone by contrasting seasonal and perennial ice floes in regions where flooding has been observed in the field. This will allow competing ice-floe signature effects to be resolved, such that the widespread nature of the snow-ice growth process may be more accurately quantified in high-resolution radar image data.

7.0 Acknowledgments

Sincere thanks go to Günter Kohlhammer, of ESA Darmstadt, who provided valuable support in planning ISW data acquisitions, and Klaus Reiniger who managed the operation of G.A.R.S and made data reception at O'Higgins a reality. Jörg Gredel, Birgit Schättler, and Gunther Schreier of D-PAF provided timely and invaluable SAR product support. Ron Kwok and Shirley Pang of JPL, and Shusun Li of ASF are also thanked for their support in developing geolocation and calibration routines, respectively. Timo Vihma kindly provided the Finnish Salargos buoy temperatures for the extension of this analysis. M.R.D completed this work at the Jet Propulsion Laboratory under contract to the National Aeronautic and Space Administration, as part of the ESA-supported ERS-1 AO PIPOR study PIP.Ant3. Robert Thomas of the Polar Branch of Mission to Planet Earth provided funding support for this work. V.I.L. completed the field portion of this research with support from NSF Grant OPP 9024809. Thanks to S. Marsland and D. Turner for help with the image processing.

8.0 References

Ackley, S.F., B. Elder, V.I. Lytle, and D. Bell, Sea-Ice Investigations On Ice Station Weddell-1: I. Ice Dynamics, *Ant. J. of the U.S.*, 5, 27, 111-113, 1992.

Allison, I., and A. Worby, Seasonal Changes Of Sea-Ice Characteristics Off East Antarctica, *Annals of Glaciology*, 20, 195-201, 1994.

Andreas, E.L., A.B. Makshtas, K.J. Claffey, and V. Ivanov, Surface Level Meteorological Conditions On Ice Station Weddell (abstract), *EOS Trans. AGU*, 73, 308, 1992.

Carsey, F.D., B. Holt, S. Martin, L. McNutt, D.A. Rothrock, V.A. Squire, and W.F. Weeks, Weddell-Scotia Sea Marginal Ice Zone Observations From Space, October 1984, *J. Geophys. Res.*, 91, C3, 3920-3924, 1986.

Cavalieri, D. J., J. P. Crawford, M. R. Drinkwater, D. T. Eppler, L. D. Farmer, R. R. Jentz, and C. C. Wackerman, Aircraft active and passive microwave validation of sea ice concentration from the Defense Meteorological Satellite Program Special Sensor Microwave Imager, *J. Geophys. Res.*, 96, C12, 21989-22008, 1991.

Comiso, J.C., T.C. Grenfell, M. Lange, A.W. Lohanick, R.K. Moore, and P. Wadhams. Microwave Remote Sensing Of The Southern Ocean Ice Cover, In *Microwave Remote Sensing of Sea Ice*, (Ed.) F.D. Carsey, AGU *Geophysical Monograph*, 28, Chapt. 12, 244-259, 1992.

Drinkwater, M.R., Satellite Microwave Radar Observations of Antarctic Sea Ice. In C. Tsatsoulis and R. Kwok (Eds.), *Recent Advances in the Analysis of SAR for Remote Sensing of the Polar Oceans*, Springer Verlag, In Press.

Drinkwater, M.R., Airborne And Satellite SAR Investigations Of Sea-Ice Surface Characteristics. In *Oceanographic Applications of Remote Sensing*, (Ed's) Ikeda, M. and Dobson, F., Chapt. 21., CRC Press, 345-364, 1995.

Drinkwater, M.R., and C. Haas, Snow, Sea-Ice And Radar Observations During ANT X/4: Summary Data Report, *Berichte aus dem Fachbereich Physik*, 53, Alfred Wegener Institut für Polar- und Meeresforschung, Bremerhaven, Germany, 58 pp., 1994.

Drinkwater, M.R., and C. Kottmeier, Satellite Microwave Radar- and Buoy-Tracked Ice Motion In The Weddell Sea During WWGS'92. *IGARSS '94*, Vol. 1, 153-155, Pasadena, CA, Aug. 8-12, IEEE Cat. No. 94CH3378-7, 1994.

Drinkwater, M.R., and F.D. Carsey, Observations Of The Late-Summer to Fall Transition With The 14.6 GHz SEASAT Scatterometer, *Proc. IGARSS '91 Symposium*, Vol. 3, IEEE Catalog #CH2971-0, June 3-6, 1991, Espoo, Finland, 1597-1600, 1991.

Drinkwater, M.R., R. Hosseinmostafa, and S.P. Gogineni, C-band Backscatter Measurements Of Winter Sea Ice in the Weddell Sea, Antarctica, *Int. J. Remote Sensing*, 16, 17, 3365-3389, 1995.

Drinkwater, M.R., D.S. Early and D.G. Long, ERS-1 Investigations of Southern Ocean Sea-ice Geophysics using Combined Scatterometer and SAR Images. *Proc. IGARSS '94*, Vol. 1, 165-168, Pasadena, CA, Aug. 8-12, IEEE Cat. No. 94CH3378-7, 1994.

Drinkwater, M.R., D.G. Long, and D.S. Early, Enhanced Resolution Scatterometer Imaging of Southern Ocean Sea Ice, *ESA Journal*, 17, 307-322, 1993.

Eicken, H., M.A. Lange, H. Hubberten, and P. Wadhams, Characteristics And Distribution Patterns Of Snow And Meteoric Ice In The Weddell Sea And Their Contribution To The Mass Balance Of Sea Ice, *Ann. Geophysicae*, 12, 80-93, 1994.

Eicken, H., H. Fischer, and P. Lemke, Effects Of The Snow Cover On Antarctic Sea Ice And Potential Modulation Of Its Response To Climate Change, *Ann. Glaciology*, 21, 369-376, 1995.

ESA Earthnet, *ERS-1 System*, ESA Special Publication, SP-1146, ESA Publications Division, ESTEC, Noordwijk, The Netherlands, 87 pp., 1992.

Fetterer, F. M., D. Ginneris, and R. Kwok, Sea Ice Type Maps From Alaska Synthetic Aperture Radar Facility Imagery: An Assessment, *J. Geophys. Res.*, 99, 11, 22443-22458, 1994.

Fritsen, C.H., V.I. Lytle, S.F. Ackley, and C.W. Sullivan, Autumn Bloom of Antarctic Pack-Ice Algae, *Science*, 266, 782-784, 1994.

Glen, J.W. and J.G. Paren, The Electrical Properties Of Snow And Ice, *J. Glaciology*, 15, 73, 15-38, 1975.

Gloersen, P., W.J. Campbell, D.J. Cavalieri, J.C. Comiso, C.L. Parkinson, and H.J. Zwally, Arctic And Antarctic Sea Ice, 1978-1987: Satellite Passive-Microwave Observations And Analysis. *NASA SP-511*, Washington DC, National Aeronautics and Space Administration, 1992.

Gogineni, S.P., R.K. Moore, T.C. Grenfell, D.G. Barber, S. Digby, and M.R. Drinkwater, The Effects of Freeze-up and Melt Processes on Microwave Signatures, In *Microwave Remote Sensing of Sea Ice*, (Ed.) F.D. Carsey, American Geophysical Union, Geophysical Monograph 28, Chapt. 17, 329-341, 1992.

Gordon, A.L., and Ice Station Weddell Group of Principal Investigators and Chief Scientists, Weddell Sea Exploration from Ice Station, *Eos*, 74, 11, 121, 1993.

Hallikainen, M., and D.P. Winebrenner, The Physical Basis for Sea Ice Remote Sensing, In *Microwave Remote Sensing of Sea Ice*, (Ed.) F.D. Carsey, American Geophysical Union, Geophysical Monograph, 28, Chapt. 3, 29-46, 1992.

Hosseinmostafa, A. R., V.I. Lytle, K.C. Jezek, S.P. Gogineni, S.F. Ackley, and R.K. Moore, Comparison Of Radar Backscatter From Antarctic And Arctic Sea Ice, *J. Electromag. Waves and Apps.*, 9, 3, 421-438, 1995.

Kawamura, T., K.I. Ohshima, T. Takizawa, and S. Ushio, Physical, Structural And Isotopic Characteristics And Growth Processes Of Sea Ice In Lützow-Holm Bay, Antarctica. *J. Geophys. Res.*, 13, Accepted for publication, July 1996.

Kwok, R., and G.F. Cunningham, Backscatter Characteristics Of The Winter Sea-Ice Cover In The Beaufort Sea, *J. Geophys. Res.*, 99, 7787-7802, 1994.

Launiainen, J., J. Uotila, K. Rantanen, and T. Vihma, Air-Sea Interaction Experiment in the Weddell Sea, 2nd Meteorological Argos-Buoy Data Report from FINNARP, 1991-1993, *Antarctic Reports of Finland*, 3, Ministry of Trade and Industry, Helsinki, 23pp., 1994a.

Launiainen, J., and T. Vihma, On the Surface Heat Fluxes in the Weddell Sea. In *The Polar Oceans and Their Role Shaping the Global Environment*, (Eds.) O.M. Johannessen, R.D. Muench, and J.E. Overland, American Geophysical Union, Geophysical Monograph, 85, 399-419, 1994b.

Laur, H., Derivation of Backscattering Coefficient σ^0 in ERS-1 SAR.PRI Products, European Space Agency Report, ESA ESRIN, 16pp, 1992.

Lytle, V., and S. Ackley, Heat Flux Through Sea Ice In The Western Weddell Sea: Convective And Conductive Transfer Processes, Submitted to *J. Geophys. Res.*, 1996.

Lytle, V.I., K.C. Jezek, S.P. Gogineni, and A.R. Hosseinmostafa, Field Observations of Microwave Backscatter from Weddell Sea Ice, *Int. J. Remote Sensing*, 17, 1, 167-180, 1996.

Long, D.L., P.J. Hardin, and P.T. Whiting, Resolution Enhancement of Spaceborne Scatterometer Data, *IEEE Trans. Geosci. and Remote Sens.*, 31, 3, 700-715, 1993.

Long, D.G., D.S. Early, and M.R. Drinkwater, Enhanced Resolution ERS-1 Scatterometer Imaging of Southern Hemisphere Polar Ice, *Proc. IGARSS '94*, Vol. 1, 156-158, Pasadena, CA, Aug. 8-12, IEEE Cat. No. 94CH3378-7, 1994.

Martin, S., B. Holt, D.J. Cavalieri, and V. Squire, Shuttle Imaging Radar B (SIR-B) Weddell Sea Ice Observations: A Comparison Of SIR-B And Scanning Multichannel Radiometer Ice Concentrations, *J. Geophys. Res.*, 92, C7, 7173-7180, 1987.

Massom, R., M.R. Drinkwater and C. Haas, Winter Snowcover on Sea Ice in the Weddell Sea, *J. Geophys. Res.*, 102 (C1), 1101-1117, 1997.

Oelke, C., Atmospheric Signatures In Sea-Ice Concentration Estimates From Passive Microwaves: Modelled and Observed, *Int. J. Remote Sens.*, In Press.

Sommerfeld, R.A., and E. LaChappelle, The Classification Of Snow Metamorphism, *J. Glaciology*, 9, 5, 3-17, 1970.

Stoffelan, A., and D.L.T. Anderson, ERS-1 Scatterometer Data Characteristics and Wind Retrieval Skill, Space at the Service of Our Environment, *Proc. 1st ERS-1 Symp.*, 4-6 Nov. 1992, Cannes, France, ESA SP-359, Vol. 1, 41-47, 1993.

Winebrenner, D.P., B. Holt, and E. D. Nelson, Observations Of Autumn Freeze-Up In The Beaufort And Chukchi Seas Using The ERS-1 Synthetic Aperture Radar, *J. Geophys. Res.*, 101, C7, 16401-16419, 1996.

Winebrenner, D.P., E.D. Nelson, and R. Colony, Observations Of Melt Onset On Multiyear Arctic Sea Ice Using The ERS 1 Synthetic Aperture Radar, *J. Geophys. Res.*, 99, 11, 2225-22441, 1994.

Figures

Figure 1 Map of the ISW-drift track, and locations of ERS-1 SAR image frames on ascending and descending orbits (see Table I). The enlarged inset indicates the period of observations in this study, together with the drift of the camp floe: air temperatures are indicated for each imaged location.

Figure 2. ERS-1 SAR images and charts depicting; (a) regional sea-ice conditions around ISW on February 10, 1992, and (b) a zoomed depiction of box region showing the bright reflection from *Akademik Fedorov* (AF) moored alongside the camp floe [SAR image data © ESA 1992]; (c) large scale roughness of the ISW camp floe characterized by the backscatter intensity of the ship-based radar. Higher numbers inside triangles indicate the rougher portions of the floe; and (d) indicates the locations of remote sites Alex, Brent, Chris, Dimitri, and Ed, on day 62.

Figure 3. Meteorological timeseries of (a) air temperature; (b) wind speed; (c) 24-hour smoothed true wind direction; and (d) surface air pressure. Data prior to day 57 is obtained from the Finnish Salargos buoy, and after day 57 (marked by symbol *) was collected at ISW.

Figure 4. Histograms indicating four contrasting pixel backscatter distributions around ISW at times, for; (1) day 38; (2) day 41; (3) day 70; and (4) day 74.

Figure 5. Relationships between the backscatter coefficients of ERS-1 SAR, $\bar{\sigma}_{SAR}^{\circ}$ ($\theta = 23^{\circ}$), scatterometer, $\bar{\sigma}_{Scat}^{\circ}$ ($\theta = 40^{\circ}$) and (a) wind speed; and (b) air temperature.

Figure 6. Measurement timeseries of (a) hourly air temperatures with SAR imaging times; (b) thermistor snow temperature gradients; (c) ERS-1 radar backscatter coefficients; ■ indicates $\bar{\sigma}_{MY}^{\circ}$ (i.e. mean multi-year ice floe value) and the range from all tracked floes; ✕ is the global SAR image mean ($\bar{\sigma}_{SAR}^{\circ}$); and ● is the 40° incidence normalised EScat backscatter coefficient ($\bar{\sigma}_{Scat}^{\circ}$); (d) linear-fitted EScat backscatter gradient (M) between 20 and 60° incidence.

Figure 7. Timeseries of the thermal profile obtained from site A on the camp floe (see Figure 2c for location), indicating the downward propagation of the freezing (-1.8°C) isotherm with time. The dotted line indicates sea level and the upper solid line the mean height of the time-varying snow depth.

Figure 8. Heuristic Model for temporal changes occurring to thick ice surviving the Antarctic austral summer through fall freeze-up. Salinity and temperature changes are described, together with the schematic relationship to the origins of C-band backscattering.

TABLES AND APPENDICES

TABLES

Table 1.

Table 2.

APPENDIX

Appendix I.

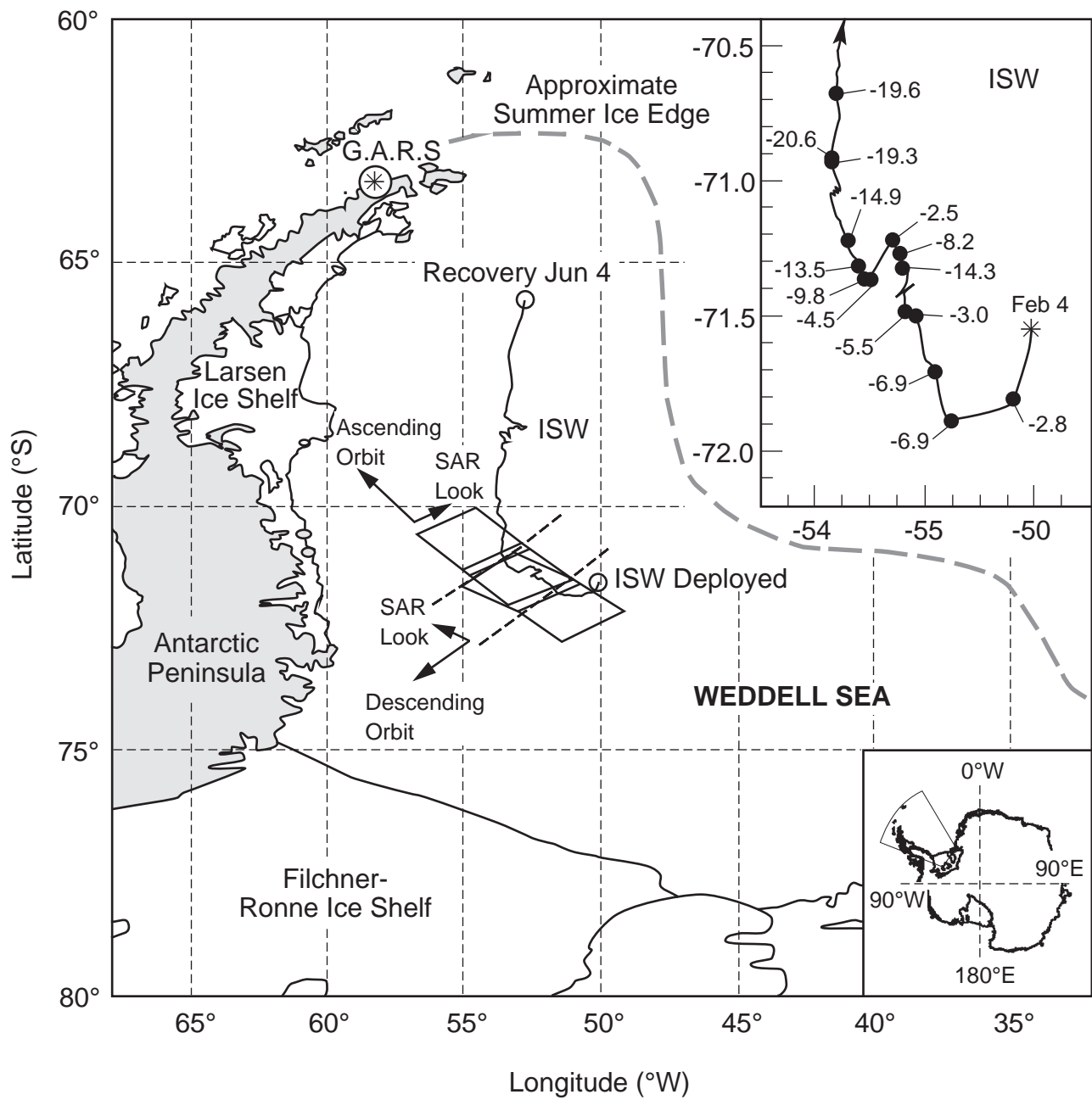
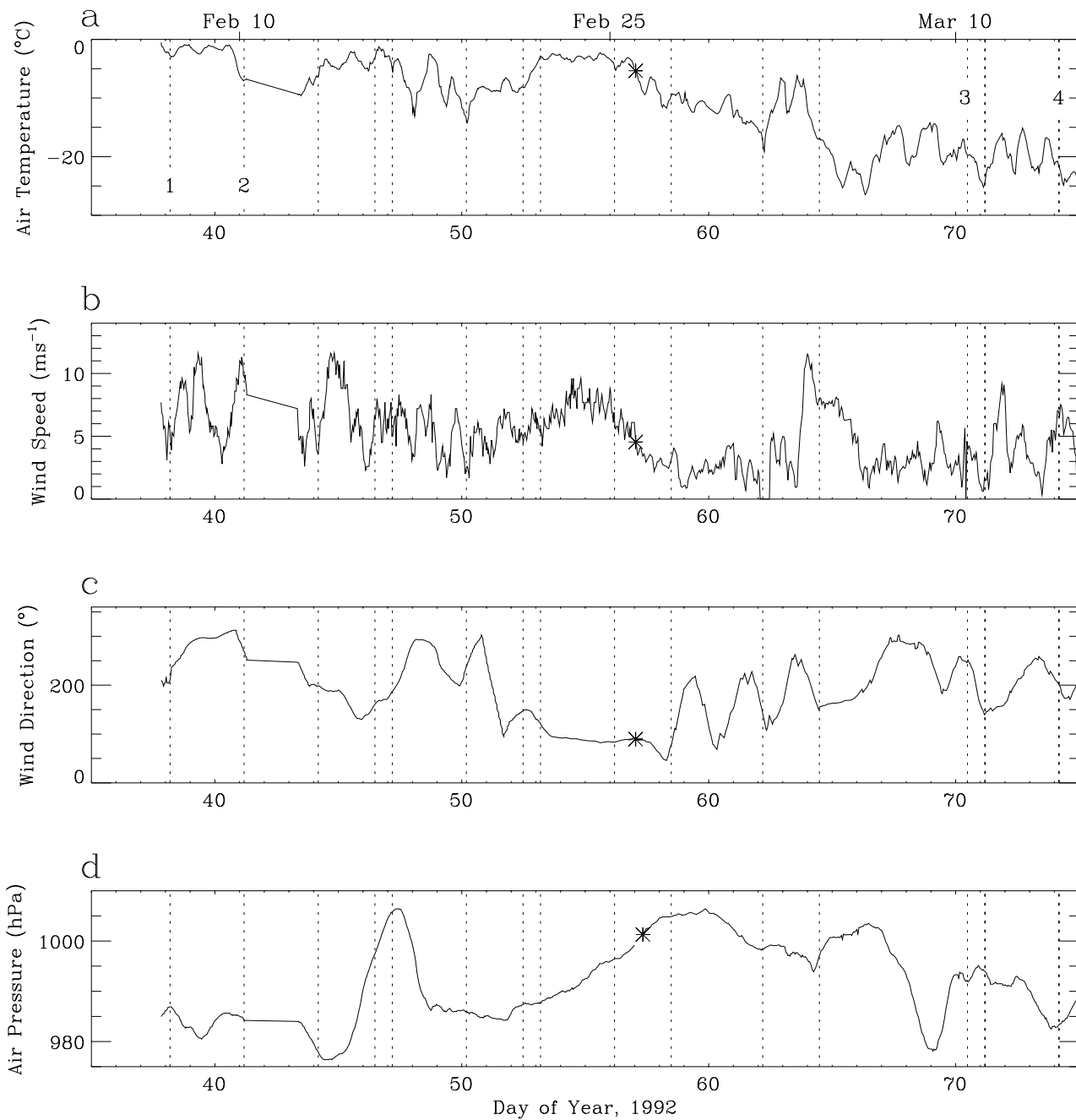
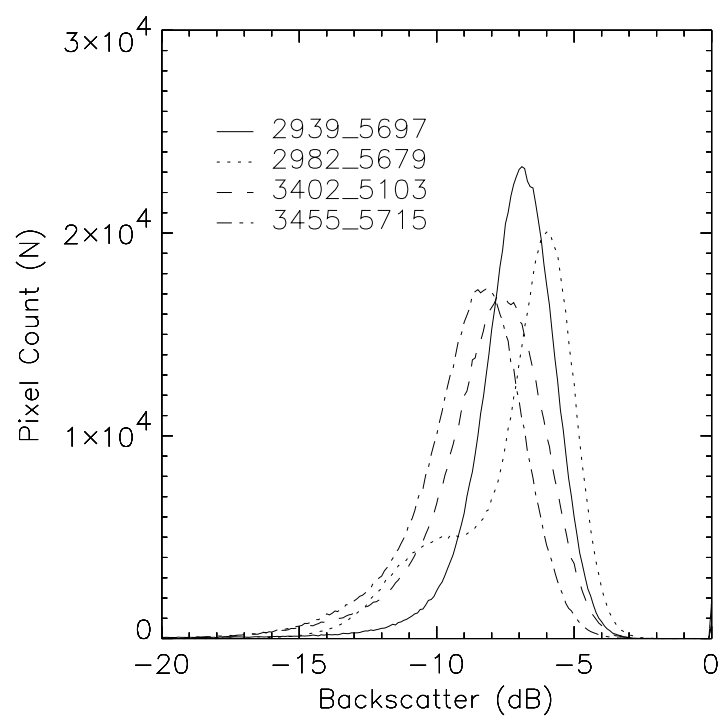
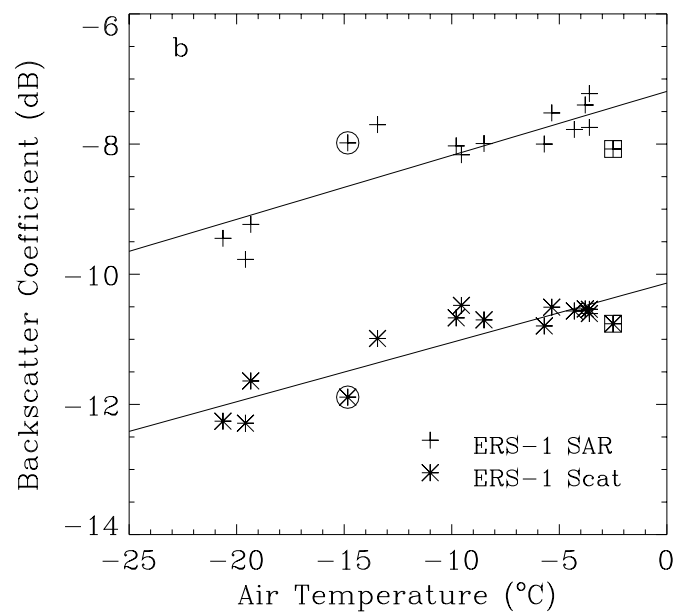
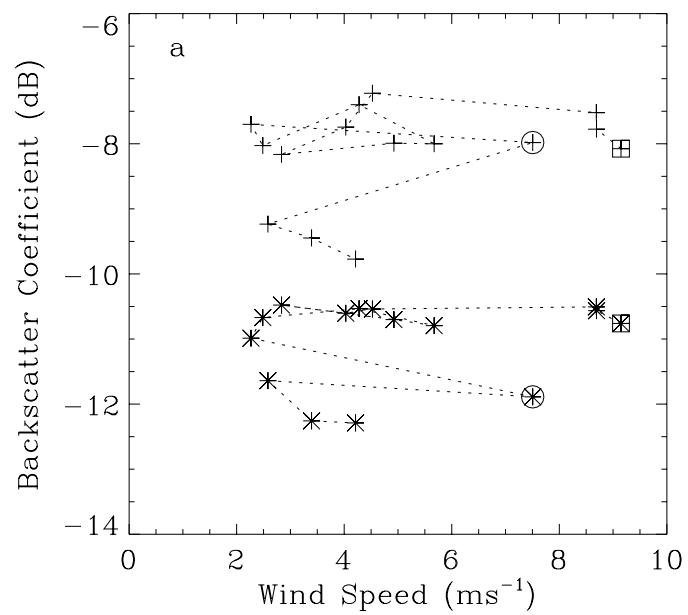
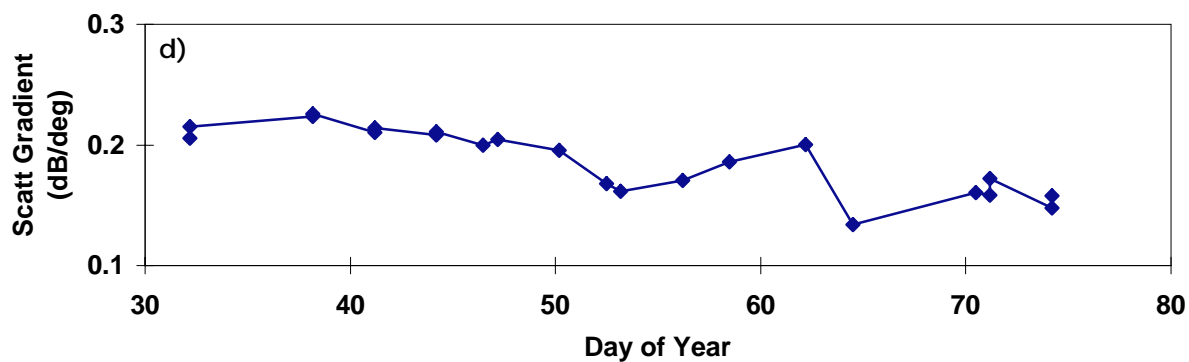
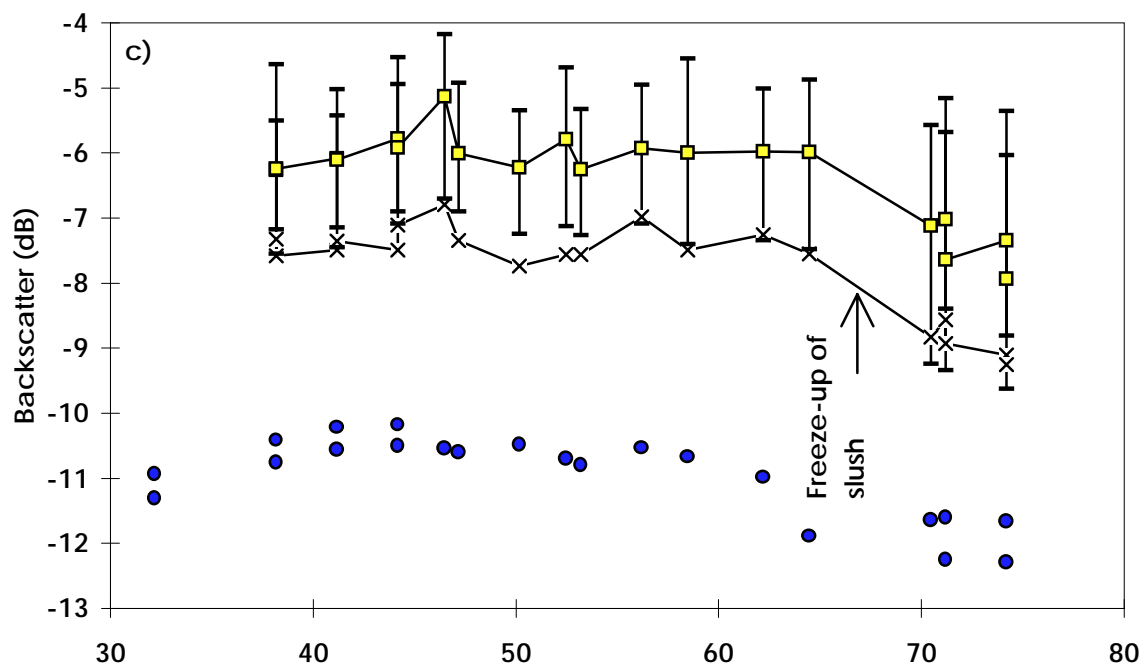
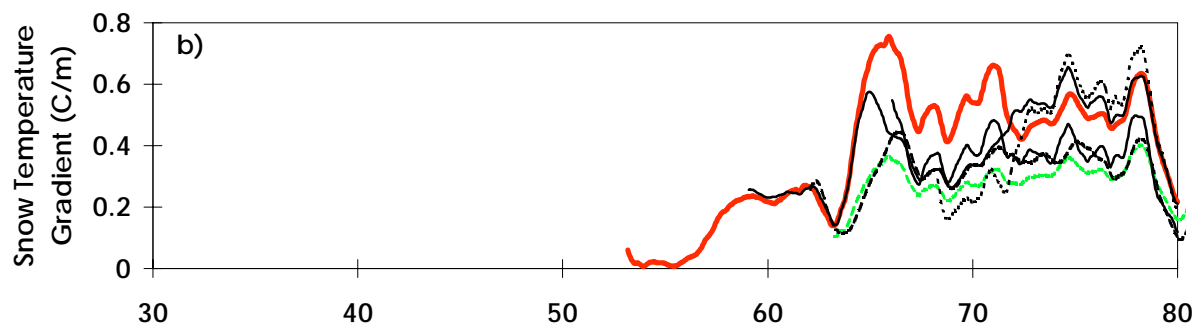
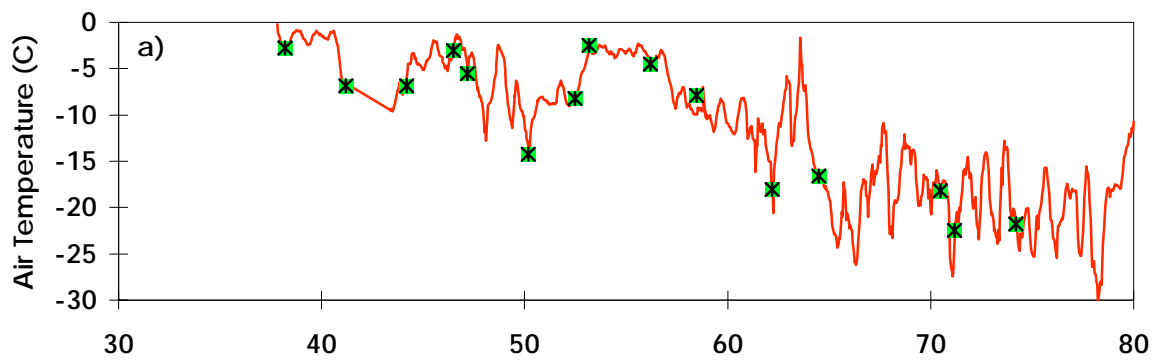


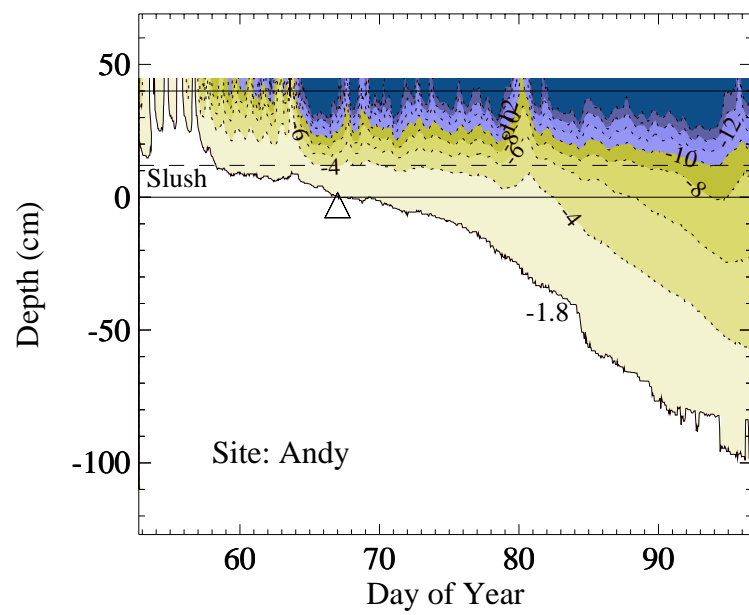
Figure 1.











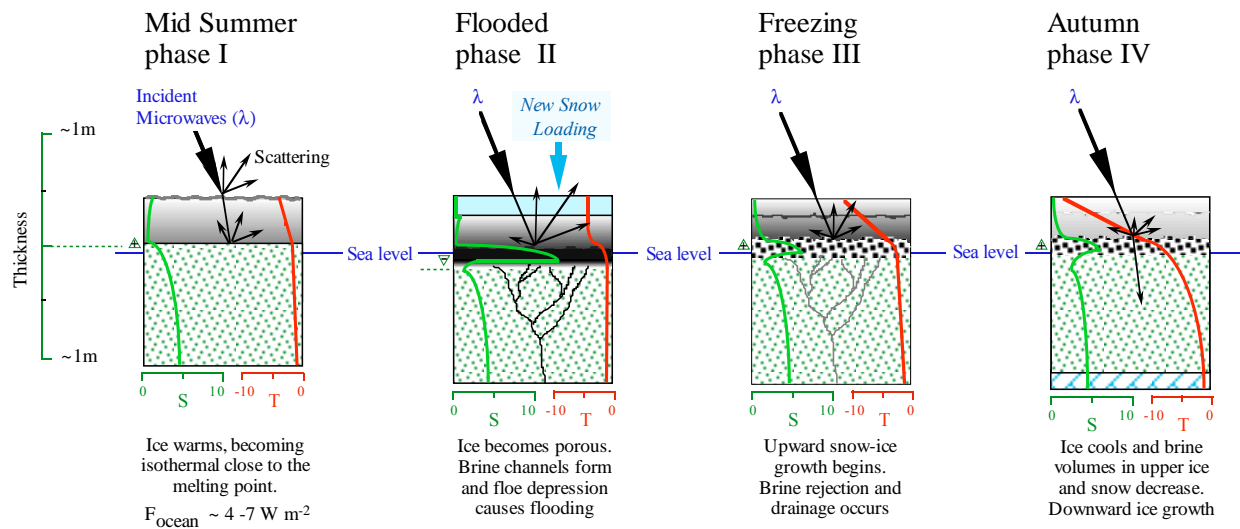
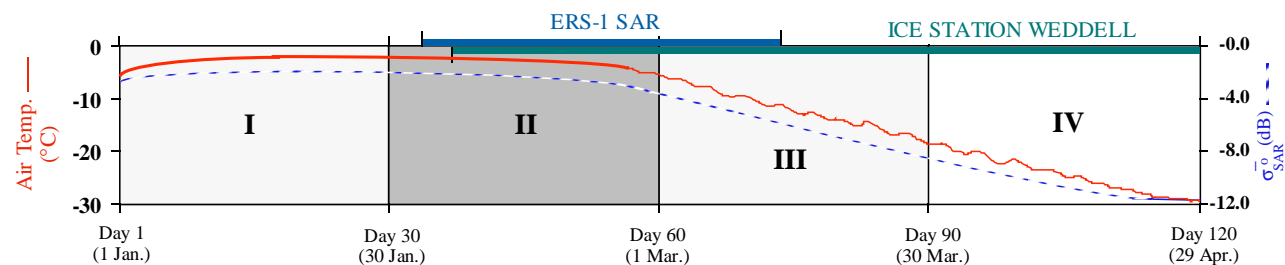


Table 1. Listing of air temperatures, and wind speeds obtained from the Finnish Salargos buoy (prior to day 57) and Ice Station Weddell, and ice concentrations obtained from supervised ERS-1 SAR data classification of images listed in Appendix I.

Decimal Day	Air Temp. (°C)	Windspeed (ms ⁻¹)	Ice Concentration	Open Water Fraction
38.2	-2.8	9.2	0.985	0.015
41.2	-6.9	8.7	0.984	0.016
44.2	-6.9	8.7	0.971	0.029
46.5	-3.0	4.5	0.910	0.089
47.2	-5.5	4.0	0.981	0.019
50.2	-14.3	2.8	0.985	0.015
52.5	-8.2	4.9	0.968	0.032
53.2	-2.5	5.7	0.987	0.013
56.2	-4.5	4.3	0.969	0.031
58.5	-9.8	2.5	0.970	0.030
62.2	-13.5	2.3	0.971	0.029
64.5	-14.9	7.5	0.969	0.031
70.5	-19.3	2.6	0.992	0.008
71.2	-20.6	3.4	0.998	0.002
74.2	-19.6	4.2	0.998	0.002

Table 2. Listing of visual ice observations during helicopter flights.
No data indicates poor visibility and lack of contrast between new ice and open water.

Date (Day of Year)	Direction of Flight	Open Water (%)	Nilas (%)
Feb 12 (43)	East	10-20	-
Feb 17 (48)	South & East	3	3
Feb 17 (48)	North	7	10
Feb 27 (58)	West	8	10-20
Feb 29 (60)	South & East	0	20
March 1 (61)	East	0	20
March 1 (61)	North	2-3	20
March 3 (63)	West (50 km)	1	20
March 3 (63)	West (100 km)	5	10
March 3 (63)	East	1	-
March 6 (66)	East	0	-
March 9 (69)	West	<1	10
March 10 (70)	South & East	0	-
March 14 (74)	East and West	-	-

Appendix I. Listing of ERS-1 SAR images used in the study, together with their orbit/frame numbers and the date and time of acquisition. Precision in time information is retained here to maintain necessary precision in locating targets within geolocated SAR images.

Image	Day + Time (GMT)		IMAGE CENTER		ISW		ERS-1 SAR	
ID#	Date	Decimal Day	Longitude	Latitude	Latitude	Longitude	orbit	frame*
1	1 Feb. 1992	32.18568464	-72.125	-51.267	-	-	2853	5679
2	1 Feb. 1992	32.18585917	-71.417	-53.080	-	-	2853	5697
3	7 Feb. 1992	38.18569878	-72.123	-51.286	-71.8222	-50.3453	2939	5679
4	7 Feb. 1992	38.18587328	-71.414	-53.099	-71.8222	-50.3453	2939	5697
5	10 Feb. 1992	41.18569747	-72.121	-51.282	-71.9058	-51.4684	2982	5679
6	10 Feb. 1992	41.18586801	-71.413	-53.094	-71.9058	-51.4684	2982	5697
7	13 Feb. 1992	44.18570231	-72.125	-51.282	-71.7283	-51.7772	3025	5679
8	13 Feb. 1992	44.18587686	-71.417	-53.095	-71.7283	-51.7772	3025	5697
9	15 Feb. 1992	46.48245574	-71.587	-53.038	-71.5335	-52.1546	3058	5103D
10	16 Feb. 1992	47.18589009	-71.415	-53.101	-71.5202	-52.3233	3068	5697
11	19 Feb. 1992	50.18588884	-71.414	-53.101	-71.3668	-52.3724	3111	5697
12	21 Feb. 1992	52.48244245	-71.587	-53.035	-71.3047	-52.4648	3144	5103D
13	22 Feb. 1992	53.18586709	-71.413	-53.096	-71.2664	-52.5471	3154	5697
14	25 Feb. 1992	56.18583784	-71.525	-52.836	-71.4122	-52.9834	3197	5697
15	27 Feb. 1992	58.48242006	-71.576	-53.069	-71.4038	-53.1045	3230	5103D
16	2 Mar. 1992	62.18585153	-71.414	-53.100	-71.3592	-53.1726	3283	5697
17	4 Mar. 1992	64.48242834	-71.589	-53.017	-71.2670	-53.3821	3316	5103D
18	10 Mar. 1992	70.48246020	-71.589	-53.029	-70.9942	-53.6072	3402	5103D
19	11 Mar. 1992	71.18589220	-71.422	-53.114	-70.9768	-53.6247	3412	5697
20	11 Mar. 1992	71.18606674	-70.698	-54.799	-70.9768	-53.6247	3412	5715
21	14 Mar. 1992	74.18588495	-71.416	-53.121	-70.7644	-53.5745	3455	5697
22	14 Mar. 1992	74.18605949	-70.693	-54.811	-70.7644	-53.5745	3455	5715

* Note Suffix D signifies SAR image acquired on a descending orbit.